Multiple charge density wave transitions in the antiferromagnets $R\mathrm{NiC_2}$ (R = Gd, Tb)

S. Shimomura,[1,*] C. Hayashi,[2] N. Hanasaki,[3] K. Ohnuma,[2] Y. Kobayashi,[2] H. Nakao,[4] M. Mizumaki,[5] and H. Onodera[6]

[1]*Department of Physics, Kyoto Sangyo University, Kyoto 603-8555, Japan*

[2]*Department of Physics, Faculty of Science and Technology, Keio University, Yokohama 223-8522, Japan*

[3]*Department of Physics, Osaka University, Toyonaka 560-0043, Japan*

[4]*Condensed Matter Research Center (CMRC) and Photon Factory, Institute of Materials Structure Science (IMSS), Tsukuba 305-0801, Japan*

[5]*Japan Synchrotron Radiation Research Institute, SPring-8, Hyogo 679-5198, Japan*

[6]*Department of Physics, Graduate School of Science, Tohoku University, Sendai 980-8578, Japan*

(Received 26 January 2016; revised manuscript received 8 March 2016; published 6 April 2016)

X-ray scattering and electrical resistivity measurements were performed on $\mathrm{GdNiC_2}$ and $\mathrm{TbNiC_2}$. We found a set of satellite peaks characterized by $\boldsymbol{q}_1 = (0.5,\eta,0)$ below T_1, at which the resistivity shows a sharp inflection, suggesting the charge density wave (CDW) formation. The value of η decreases with decreasing temperature below T_1, and then a transition to a commensurate phase with $\boldsymbol{q}_{1\mathrm{C}} = (0.5,0.5,0)$ takes place. The diffuse scattering observed above T_1 indicates the presence of soft phonon modes associated with CDW instabilities at $\boldsymbol{q}_1$ and $\boldsymbol{q}_2 = (0.5,0.5,0.5)$. The long-range order given by $\boldsymbol{q}_2$ is developed in addition to that given by $\boldsymbol{q}_{1\mathrm{C}}$ in $\mathrm{TbNiC_2}$, while the short-range correlation with $\boldsymbol{q}_2$ persists even at 6 K in $\mathrm{GdNiC_2}$. The amplitude of the $\boldsymbol{q}_{1\mathrm{C}}$ lattice modulation is anomalously reduced below an antiferromagnetic transition temperature T_N in $\mathrm{GdNiC_2}$. In contrast, the $\boldsymbol{q}_2$ order vanishes below T_N in $\mathrm{TbNiC_2}$. We demonstrate that $R\mathrm{NiC_2}$ (R = rare earth) compounds exhibit similarities with respect to their CDW phenomena, and discuss the effects of magnetic transitions on CDWs. We offer a possible displacement pattern of the modulated structure characterized by $\boldsymbol{q}_{1\mathrm{C}}$ and $\boldsymbol{q}_2$ in terms of frustration.

DOI: 10.1103/PhysRevB.93.165108

I. INTRODUCTION

Low-dimensional systems exhibit remarkable properties associated with instabilities in the electronic structure, such as charge density wave (CDW) and spin density wave [1,2]. The CDW occurs in low-dimensional metal systems with electron-lattice coupling. The nesting of the Fermi surface leads to electronic instability, resulting in a charge density modulation accompanied by a periodic lattice distortion characterized by $2k_\mathrm{F}$, where k_F is the Fermi wave vector. Competition or cooperation among different types of orders has recently attracted considerable attention in condensed matter physics. The interplay between CDW and superconductivity has been studied extensively. Investigations of the interplay between CDW and magnetism have also led to an improved understanding of the interplay among different types of orders and to the elucidation of various exotic phenomena. The interplay between CDW and magnetism may be realized in low-dimensional metal compounds containing rare-earth elements, in which the crystal lattice, conduction electrons, and $4f$ magnetic moments should interact with one another through, for example, the RKKY, electron-lattice, and magnetoelastic interactions. Some rare-earth compounds, such as $\mathrm{Er_5Ir_4Si_{10}}$, exhibiting CDW transitions have been reported, but there is no evident coupling between CDW and magnetism [3–6].

Recently we observed intriguing behaviors involving the interplay between CDW and ferromagnetism in the intermetallic compound $\mathrm{SmNiC_2}$ [7]. The electrical resistivity along $\boldsymbol{a}$ (ρ_a), $\boldsymbol{b}$ (ρ_b), and $\boldsymbol{c}$ (ρ_c) shows a sharp inflection at $T_1 = 148$ K and a discontinuous change at ferromagnetic transition temperature $T_\mathrm{C} = 17.7$ K, as shown in Fig. 1 [7]. X-ray diffraction measurements revealed that a set of satellite peaks characterized by an incommensurate wave vector $\boldsymbol{q}_1 = (0.5,\eta,0)$ appears below T_1. The diffuse scattering observed above T_1 has peaks characterized by $\boldsymbol{q}_1$ and another wave vector $\boldsymbol{q}_2 = (0.5,0.5,0.5)$. This indicates the softening of the phonon modes. The $\boldsymbol{q}_1$ satellite peaks and $\boldsymbol{q}_2$ diffuse scattering peaks disappear abruptly below T_C. These results indicate that $\mathrm{SmNiC_2}$ exhibits the destruction of the long-range CDW order and short-range CDW correlation in coincidence with the ferromagnetic transition. First-principles calculations of the electronic structures of $\mathrm{SmNiC_2}$ indicated the Fermi surface nesting and the divergence of the electronic susceptibility for $\boldsymbol{q}_1$ and $\boldsymbol{q}_2$, supporting the CDW instabilities [8]. High-resolution photoemission spectroscopy [9] and optical reflectivity [10] measurements revealed a gap opening attributable to the CDW formation.

The compound $\mathrm{SmNiC_2}$ is a member of the $R\mathrm{NiC_2}$ family (R denotes a rare-earth metal element), which has a noncentrosymmetric A-centered orthorhombic lattice (space group $Amm2$), as shown in Fig. 2 [11–14]. The crystal structure can be described as a stacking of layers along $\boldsymbol{c}$ composed of R and Ni atoms, whose respective positions are (0,0,0) and $(0.5,0.5,z)$ with $z \approx 0.11$. Carbon atoms, which form $\mathrm{C_2}$ units, are located between the layers [14]. The lattice constants of, for example, $\mathrm{SmNiC_2}$ are $a = 3.7037(3)$, $b = 4.5279(2)$, and $c = 6.0947(4)$ Å at room temperature [14]. According to the structure determination of the incommensurate phase of $\mathrm{SmNiC_2}$ by Wölfel *et al.* [14], Ni atoms are displaced along $\boldsymbol{a}$ with the largest modulation amplitude, and chains of Ni atoms along $\boldsymbol{a}$ should account for the quasi-one-dimensional character and carry the CDW. As proposed by Wölfel *et al.* [14], the A center would provide frustration between chains of Ni atoms in neighboring layers for the modulation with the commensurate wave vector (0.5,0.5,0), and the

*susumu@cc.kyoto-su.ac.jp

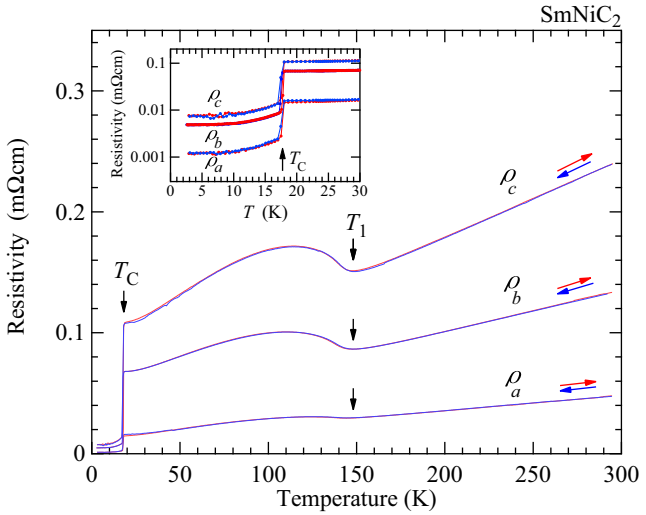

FIG. 1. Temperature dependence of the electrical resistivity of $SmNiC_2$ along $\boldsymbol{a}$ (ρ_a), $\boldsymbol{b}$ (ρ_b), and $\boldsymbol{c}$ (ρ_c) [7]. The sharp inflection at T_1 is attributable to the CDW formation. The inset shows ρ_a, ρ_b, and ρ_c below 30 K.

frustration would be responsible for the incommensurate modulation.

In contrast to $SmNiC_2$ [15–18], which exhibits the ferromagnetic transition, most of the $RNiC_2$ compounds develop antiferromagnetic ordering [15,19–28]. Their magnetic properties are governed by $4f$ moments of R^{3+} ions due to the absence of a magnetic moment on Ni atoms, and $LaNiC_2$ is nonmagnetic and exhibits superconductivity [29–34]. Early electrical resistivity measurements on polycrystalline samples of $GdNiC_2$ and $TbNiC_2$ showed anomalous temperature dependences suggestive of the CDW formation and additional transitions [35]. The resistivity data, however, appear to be inadequate to examine the changes in resistivity above and below T_N. Magnetization and neutron diffraction measurements on $TbNiC_2$ showed an antiferromagnetic transition at $T_N = 25$ K

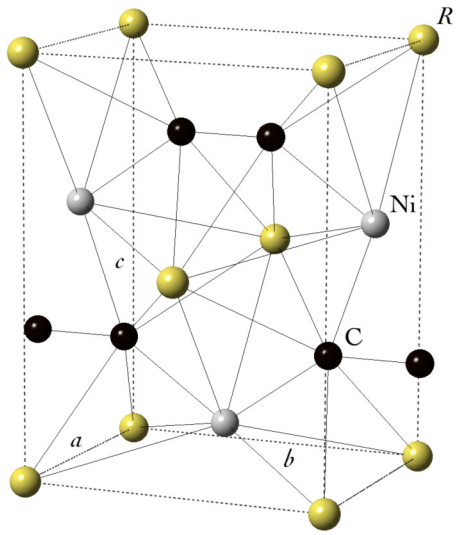

FIG. 2. Crystal structure of $RNiC_2$ (R denotes a rare-earth metal element) [11–14].

and its magnetic structure with a wave vector (0.5,0.5,0) [25–28]. The antiferromagnetic transition takes place at $T_N = 20$ K in $GdNiC_2$ [24]. Investigations into the behaviors of CDW in these compounds exhibiting the antiferromagnetic orders are needed for a comprehensive understanding of the interplay between CDW and magnetism.

To investigate the CDW phenomena of $RNiC_2$ and to examine the interplay between CDWs and antiferromagnetic orders, we have performed electrical resistivity, x-ray diffraction, and x-ray diffuse scattering measurements on $GdNiC_2$ and $TbNiC_2$. We present in Secs. III A and III B the experimental results for $GdNiC_2$ and $TbNiC_2$, respectively. We found that the lattice modulation with $\boldsymbol{q}_1 = (0.5,\eta,0)$, which is attributable to the CDW formation, is developed below T_1, and a transition to a commensurate phase with $\boldsymbol{q}_{1C} = (0.5,0.5,0)$ takes place at T_{1C} in $GdNiC_2$ and $TbNiC_2$. The long-range order with $\boldsymbol{q}_2 = (0.5,0.5,0.5)$ is additionally developed below T_2 in $TbNiC_2$. The $\boldsymbol{q}_2$ long-range order suddenly disappears below T_N, while the $\boldsymbol{q}_{1C}$ order remains. In contrast, the $\boldsymbol{q}_{1C}$ lattice modulation is suppressed below T_N in $GdNiC_2$. In Sec. IV A we summarize our experimental results concerning CDW transitions in $GdNiC_2$, $TbNiC_2$, and $SmNiC_2$ [7], and present similarities among the CDW phenomena of $RNiC_2$. We describe CDW instabilities on the basis of the results of the diffuse scattering measurements in Sec. IV B, and discuss the effects of magnetic transitions on CDWs in Sec. IV C. We offer in Sec. IV D a possible displacement pattern of the modulated structure characterized by $\boldsymbol{q}_{1C}$ and $\boldsymbol{q}_2$ in terms of frustration. Section V concludes the paper.

II. EXPERIMENT

The compounds $GdNiC_2$ and $TbNiC_2$ were synthesized by a procedure reported previously [15,23–25]. The obtained ingots consisted of a large number of single-crystal grains. The crystal orientation and single-crystalline nature were determined using the Laue photograph method. dc electrical resistivity was measured by the four-probe method in the temperature range between 2.9 and 300 K using a closed-cycle refrigerator. For these electrical resistivity measurements, each sample was cut so that most of the sample volume was a favorable domain. The typical sample size was $3.6 \times 0.5 \times 0.6$ mm^3.

We performed x-ray experiments on $GdNiC_2$ and $TbNiC_2$ using synchrotron radiation at BL-3A at the Photon Factory and at BL46XU at SPring-8, respectively. Samples of $GdNiC_2$ and $TbNiC_2$ were cut so that the widest face was parallel to the (010) plane and the (100) plane, respectively. The typical sample size was $1.7 \times 1.2 \times 0.6$ mm^3. Each sample was attached to a cold finger of the closed-cycle refrigerator. The incident x-ray energy was 13.0 keV for the measurements on $GdNiC_2$ and 18.0 keV for those on $TbNiC_2$. A four-circle diffractometer was used in each of the measurements. The intensity data were collected by a scintillation detector. The observed intensity was normalized by the intensity of the incident beam, which was monitored using an ionization chamber. The opening of the aperture in front of the detector was 0.4×0.4 mm^2. The mosaic spreads of the $GdNiC_2$ and $TbNiC_2$ samples were about 0.2° and 0.04° as determined by the full width at the half maximum of the 060 and 600 Bragg peaks, respectively. The values of the half width at the half maximum (HWHM)

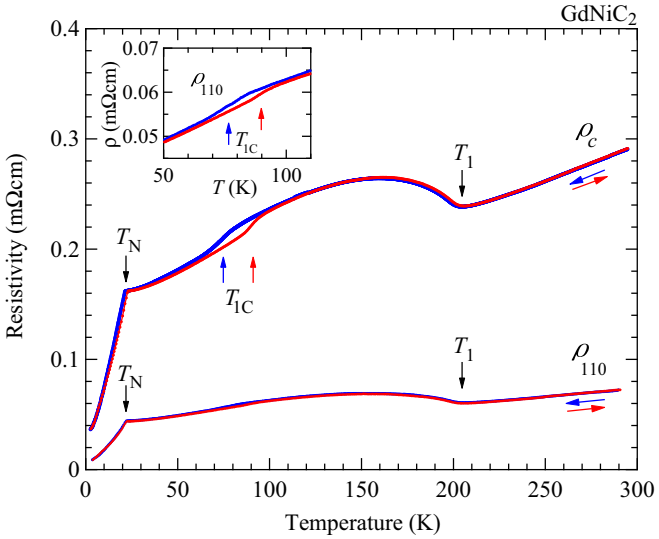

FIG. 3. Temperature dependence of the electrical resistivity of $GdNiC_2$. The resistivity measured along the c axis and that along the (1,1,0) reciprocal lattice vector perpendicular to the c axis are denoted by ρ_c and ρ_{110}, respectively. The inset shows ρ_{110} around T_{1C}.

of the 060 Bragg peak along the reciprocal lattice vectors $\boldsymbol{a}^*$, $\boldsymbol{b}^*$, and $\boldsymbol{c}^*$ in the measurements on $GdNiC_2$, defined as the experimental resolution, were about $0.0090a^*$ ($\approx$0.016 Å^{-1}), $0.0016b^*$ ($\approx$0.0022 Å^{-1}), and $0.0083c^*$ ($\approx$0.0085 Å^{-1}), respectively. The values of the HWHM of the 600 Bragg peak along $\boldsymbol{a}^*$, $\boldsymbol{b}^*$, and $\boldsymbol{c}^*$ in the measurements on $TbNiC_2$ were about $0.0020a^*$ ($\approx$0.0036 Å^{-1}), $0.0029b^*$ ($\approx$0.0041 Å^{-1}), and $0.0057c^*$ ($\approx$0.0059 Å^{-1}), respectively. Most of the x-ray measurements were carried out upon heating.

III. RESULTS

A. $GdNiC_2$

Figure 3 displays the temperature dependence of the electrical resistivity of $GdNiC_2$. The resistivity was measured along the c axis (ρ_c) and the (1,1,0) reciprocal lattice vector (ρ_{110}) perpendicular to the c axis. The value of ρ_c/ρ_{110} estimated by the data obtained at 290 K is about 4.0, which is similar to the values of $\rho_c/\rho_a \approx 5.0$ and $\rho_c/\rho_b \approx 2.8$ obtained for $SmNiC_2$ (Fig. 1) [7]. The ρ_c and ρ_{110} curves are qualitatively similar. A sharp inflection suggestive of the CDW formation is seen at $T_1 = 205$ K. The electrical resistivity increases and then decreases with decreasing temperature below T_1, indicating a partial CDW gap opening due to the imperfect nesting of the Fermi surface. An additional anomaly can be seen at 90 K for heating and at 76 K for cooling. Evident thermal hysteresis shows a first-order transition at T_{1C}. The electrical resistivity shows a sharp inflection at T_N, which is determined as 22.3 K for heating and 21.5 K for cooling. The electrical resistivity decreases more steeply with decreasing temperature below T_N.

The x-ray diffraction and diffuse scattering measurements were performed. We found a set of satellite peaks indicative of the CDW formation. Figure 4(a) displays typical satellite peak profiles along the reciprocal lattice vector $\boldsymbol{b}^*$ passing through (0.5,5.5,0) at various temperatures. The satellite peak

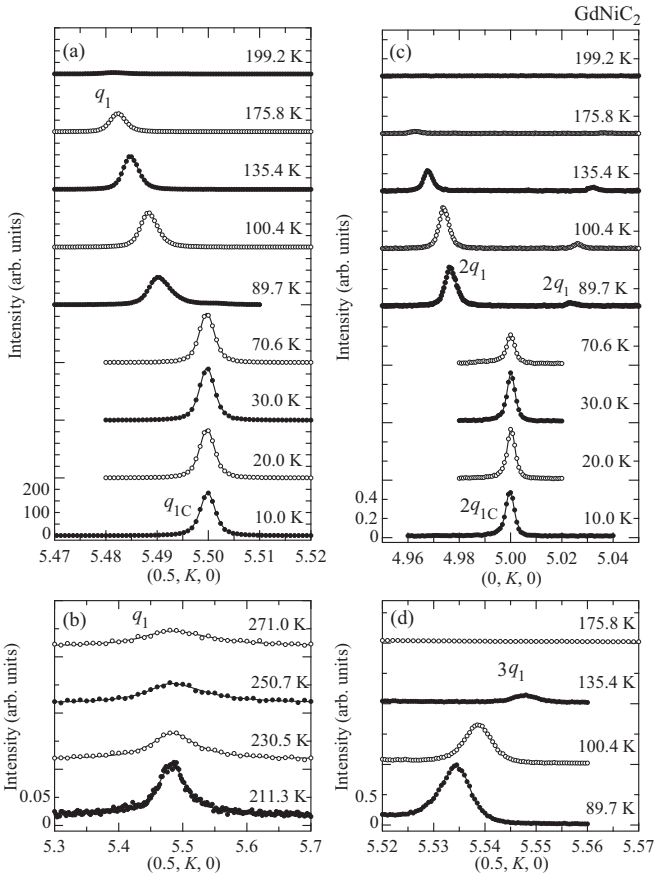

FIG. 4. Profiles of satellite peaks and diffuse scattering at several temperatures in $GdNiC_2$. (a) A satellite peak, characterized by $\boldsymbol{q}_1 = (0.5,\eta,0)$ or $\boldsymbol{q}_{1C} = (0.5,0.5,0)$, measured along $\boldsymbol{b}^*$ passing through (0.5,5.5,0). (b) Diffuse scattering measured above T_1. (c) Second-order satellite peaks given by $2\boldsymbol{q}_1$ and $2\boldsymbol{q}_{1C}$. (d) A third-order satellite peak given by $3\boldsymbol{q}_1$.

appears below T_1 at an incommensurate position $(0.5,6-\eta,0)$, which is described by the modulation wave vector $\boldsymbol{q}_1 = (0.5,\eta,0)$. With decreasing temperature from 199.2 K, the satellite peak increases its intensity and shifts its position toward the lower value of η. The peak is locked into a value of $\eta = 0.5$, corresponding to $\boldsymbol{q}_{1C} = (0.5,0.5,0)$, below T_{1C}, which is identified as an incommensurate-commensurate transition temperature. Note that the $\boldsymbol{q}_{1C}$ satellite peak persists even below T_N.

Well-defined diffuse scattering centered at the position given by $\boldsymbol{q}_1$ exists above T_1, as shown in Fig. 4(b). The diffuse scattering increases its intensity as the temperature decreases toward T_1, and then it develops into the $\boldsymbol{q}_1$ satellite peak below T_1. Second-order ($2\boldsymbol{q}_1$ and $2\boldsymbol{q}_{1C}$) and third-order ($3\boldsymbol{q}_1$) satellite peaks were observed as shown in Figs. 4(c) and 4(d), respectively.

The temperature dependence of the value of η, evaluated from the position of the $\boldsymbol{q}_1$ satellite peak, is shown in Fig. 5(a). Values of η obtained from the peak positions of the $2\boldsymbol{q}_1$ and $3\boldsymbol{q}_1$ satellites agreed with the data shown in Fig. 5(a) within the experimental uncertainty. The value of η decreases monotonically as the temperature decreases below T_1, and then it takes the commensurate value of 0.5 below T_{1C}. As shown in

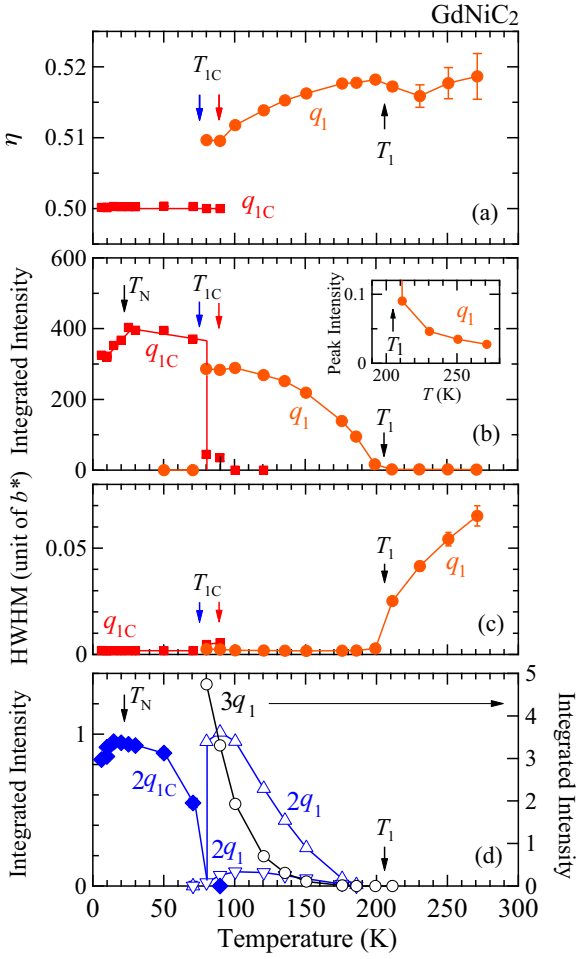

FIG. 5. Temperature dependences of (a) η, (b) integrated intensity, (c) half width at the half maximum (HWHM) of the $\boldsymbol{q}_1$ and $\boldsymbol{q}_{1C}$ peaks, and (d) integrated intensities of the second-order ($2\boldsymbol{q}_1$ and $2\boldsymbol{q}_{1C}$) and third-order ($3\boldsymbol{q}_1$) satellite peaks in $GdNiC_2$. The inset of (b) shows the diffuse scattering intensity centered at $(0.5,6-\eta,0)$.

Fig. 3, the resistivity decreases when the incommensurate-to-commensurate transition takes place. The commensurate wave vector would not correspond to an optimum nesting condition, and the restoration of a small portion of the Fermi surface would lead to the increase in the density of states.

The inset of Fig. 5(b) displays the peak intensity of the diffuse scattering centered at the position given by $\boldsymbol{q}_1$. The diffuse scattering intensity increases as the temperature decreases toward T_1, and the HWHM decreases and reaches the experimental resolution at T_1 [Fig. 5(c)]. The intensity of diffuse scattering arising from phonons (thermal diffuse scattering) is known to be approximately proportional to kT/ω^2 for $\hbar\omega/(kT) \ll 1$, where ω is the phonon frequency, $\hbar$ is the reduced Plank constant, and k is the Boltzmann constant [36]. The development of the diffuse scattering agrees with the idea that the critical phonon softening leads to the CDW order [1,2].

Figure 5(b) shows the temperature dependences of the integrated intensities of the $\boldsymbol{q}_1$ and $\boldsymbol{q}_{1C}$ satellite peaks. The intensity increases monotonically with decreasing temperature below T_1, as expected from the evolution of a gap of

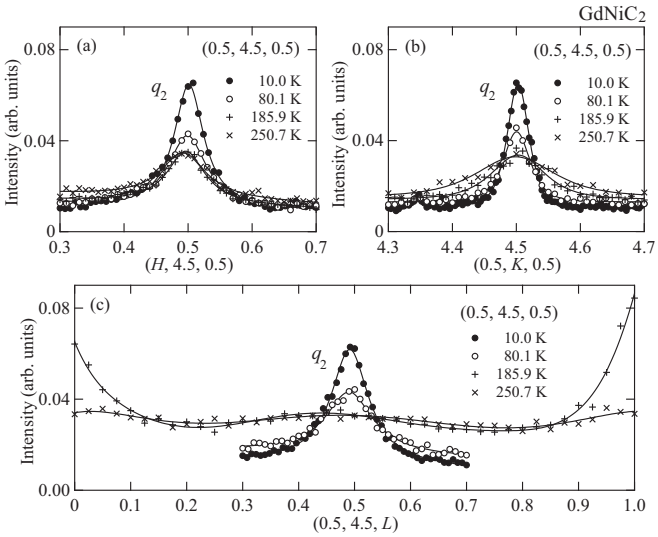

FIG. 6. Diffuse scattering profiles centered at (0.5,4.5,0.5), characterized by $\boldsymbol{q}_2 = (0.5,0.5,0.5)$, along (a) $\boldsymbol{a}^*$, (b) $\boldsymbol{b}^*$, and (c) $\boldsymbol{c}^*$ at several temperatures in $GdNiC_2$.

conventional CDW systems [1,2]. The coexistence of the $\boldsymbol{q}_1$ and $\boldsymbol{q}_{1C}$ peaks around T_{1C} was observed within the hysteresis region. The intensity of the $\boldsymbol{q}_{1C}$ satellite peak shows a sharp inflection at T_N. The intensity decreases with decreasing temperature below T_N, accompanied by a sharp decrease in the resistivity; the CDW lattice modulation is reduced as the antiferromagnetic order is developed. The values of HWHM [Fig. 5(c)] show that the long-range order persists even below T_N.

Figure 5(d) shows the temperature dependences of the integrated intensities of the second-order and third-order satellite peaks. The $2\boldsymbol{q}_1$ and $3\boldsymbol{q}_1$ satellite peaks grow more rapidly compared to the first-order $\boldsymbol{q}_1$ satellite peak for lowering temperature, indicating the squaring-up of the incommensurate CDW lattice modulation well below T_1.

A diffuse scattering peak centered at the position given by another wave vector $\boldsymbol{q}_2 = (0.5,0.5,0.5)$ was observed. Profiles of a peak centered at (0.5,4.5,0.5), characterized by $\boldsymbol{q}_2$, along $\boldsymbol{a}^*$, $\boldsymbol{b}^*$, and $\boldsymbol{c}^*$ are shown in Figs. 6(a)–6(c), respectively. The peak, which is well defined along $\boldsymbol{a}^*$ and $\boldsymbol{b}^*$, grows with decreasing temperature. The peak profiles observed along $\boldsymbol{c}^*$ at 185.9 and 250.7 K are significantly broadened. The increases in the intensity around $L = 0$ and $L = 1$ probably arise from the contribution of the diffuse scattering or satellite peaks at $(0.5,4+\eta,0)$ and $(0.5,5-\eta,1)$, respectively, which are characterized by $\boldsymbol{q}_1$. The intensity distribution of the diffuse scattering observed above T_1 likely passes through the positions given by $\boldsymbol{q}_1$ and $\boldsymbol{q}_2$. A similar intensity distribution of diffuse scattering was observed in $SmNiC_2$ [7] and in $TbNiC_2$, as described in Sec. III B.

Figures 7(a) and 7(b) illustrate the temperature dependences of the intensity and HWHM of the peak at (0.5,4.5,0.5) given by $\boldsymbol{q}_2$, respectively. Reliable values of HWHM along $\boldsymbol{c}^*$ were not obtained above 150 K owing to the significant broadening of the profiles. The values of HWHM along $\boldsymbol{a}^*$, $\boldsymbol{b}^*$, and $\boldsymbol{c}^*$ decrease monotonically with decreasing temperature, but do not reach the experimental resolution: the intrinsic values of

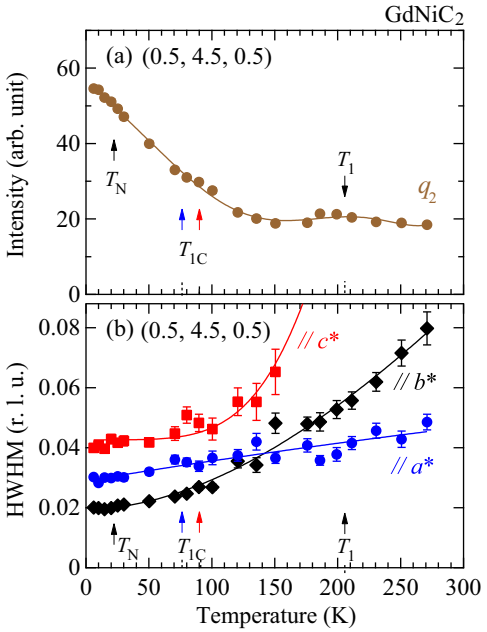

FIG. 7. Temperature dependences of (a) the intensity and (b) HWHM of the peak at (0.5,4.5,0.5) in $GdNiC_2$. The unit of the vertical axis of (b) is the reciprocal lattice unit (r.l.u.). The solid lines are guides to the eye.

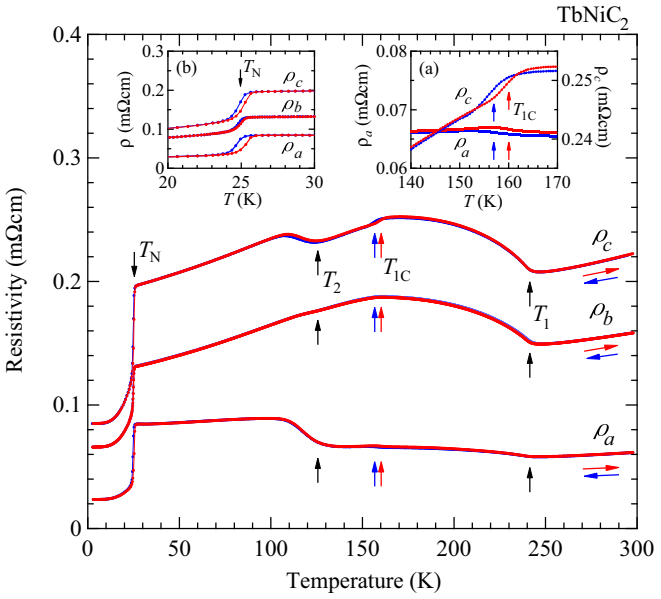

FIG. 8. Temperature dependences of the electrical resistivity along $\boldsymbol{a}$ (ρ_a), $\boldsymbol{b}$ (ρ_b), and $\boldsymbol{c}$ (ρ_c) in $TbNiC_2$. The inset (a) shows the temperature dependences of ρ_a and ρ_c around T_{1C}, and the inset (b) displays those of ρ_a, ρ_b, and ρ_c around T_N.

HWHM at the lowest temperature, obtained by subtracting each experimental resolution, are $0.022a^*$, $0.018b^*$, and $0.030c^*$, respectively. The diffuse scattering peaks given by $\boldsymbol{q}_2$, as well as those given by $\boldsymbol{q}_1$, probably originate from the phonon softening relevant to the CDW instabilities. However, the monotonic increase in the intensity with decreasing temperature below about 120 K would not be explained only by the thermal diffuse scattering [36]. The short-range correlation with $\boldsymbol{q}_2$, whether static or dynamic, would be developed at lower temperatures. Note that no apparent anomalies in intensity or HWHM can be seen at T_1, T_{1C}, or T_N.

B. $TbNiC_2$

We also performed the electrical resistivity, x-ray diffraction, and x-ray diffuse scattering measurements on $TbNiC_2$. Figure 8 shows the temperature dependences of the electrical resistivity along $\boldsymbol{a}$ (ρ_a), $\boldsymbol{b}$ (ρ_b), and $\boldsymbol{c}$ (ρ_c). The electrical resistivity shows an anisotropy with the ratios of $\rho_c/\rho_a \approx 3.6$ and $\rho_b/\rho_a \approx 2.6$ estimated by the data obtained at 290 K. These ratios are similar to those of $SmNiC_2$ and $GdNiC_2$. The ρ_a, ρ_b, and ρ_c curves show a sharp inflection at $T_1 = 243$ K. As shown in the inset (a) of Fig. 8, an apparent anomaly in each ρ_a and ρ_c curve is seen at T_{1C}, which is 160 K for heating and 157 K for cooling. An additional anomaly in each ρ_a, ρ_b, and ρ_c curve is seen at $T_2 = 128$ K in $TbNiC_2$, unlike the case in $GdNiC_2$ and $SmNiC_2$ [7]. As shown in the inset (b) of Fig. 8, the electrical resistivity discontinuously changes at T_N, which is estimated as 25.2 K for heating and 24.7 K for cooling.

The appearance of satellite peaks and the lock-in behavior were observed in $TbNiC_2$ as well as $GdNiC_2$. As shown in Fig. 9(a), one of the peaks, which is located at $(5.5,\eta,0)$ with $\eta \approx 0.519$ at 240 K, grows and shifts its position with decreasing temperature. The position of the $\boldsymbol{q}_1$ satellite peak is locked into the commensurate position of (5.5,0.5,0) characterized by $\boldsymbol{q}_{1C} = (0.5,0.5,0)$ below T_{1C}. Note that the $\boldsymbol{q}_{1C}$ satellite peak exists even below T_N. Second-order ($2\boldsymbol{q}_1$) and third-order ($3\boldsymbol{q}_1$) satellite peaks were also observed as shown in Figs. 9(b) and 9(a), respectively.

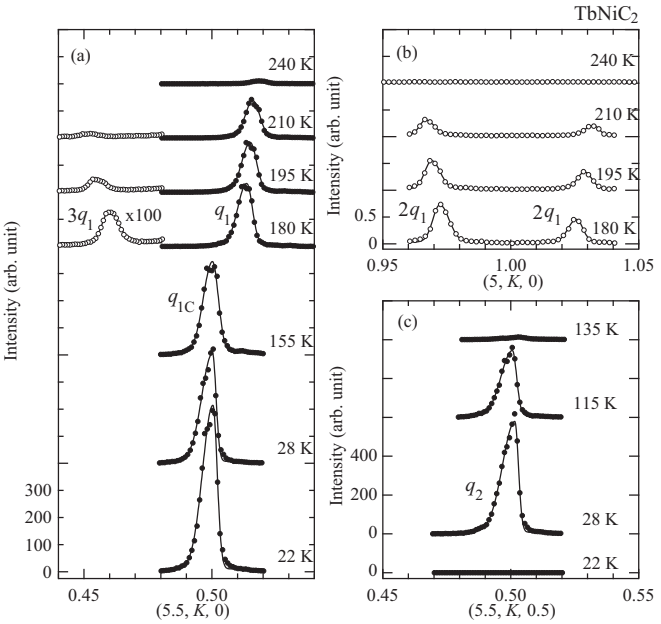

FIG. 9. (a) Satellite peak profiles characterized by $\boldsymbol{q}_1$, $\boldsymbol{q}_{1C}$, and $3\boldsymbol{q}_1$ measured along $\boldsymbol{b}^*$ at several temperatures in $TbNiC_2$. (b) Satellite peak profiles characterized by $2\boldsymbol{q}_1$. (c) Another satellite peak at (5.5,0.5,0.5) characterized by $\boldsymbol{q}_2 = (0.5,0.5,0.5)$ appears below T_2, but it vanishes below T_N.

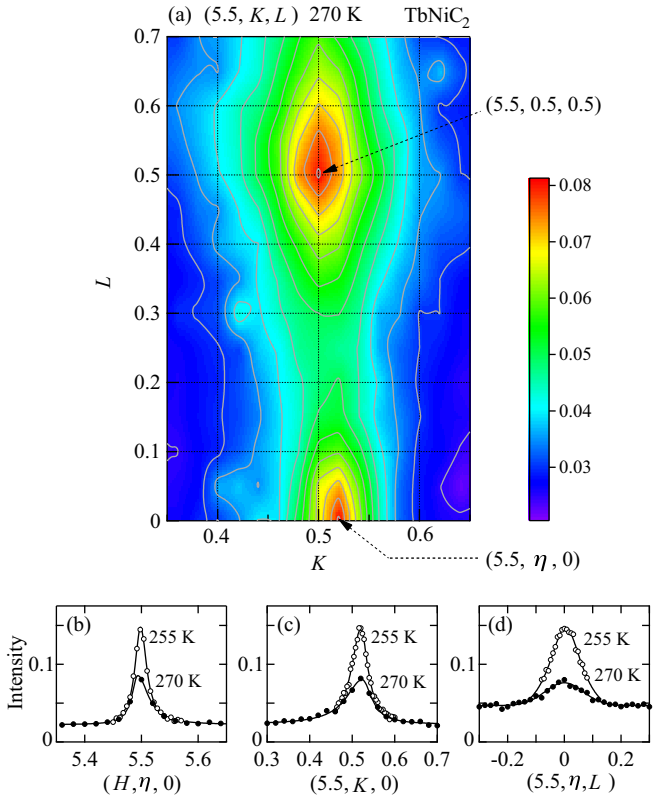

FIG. 10. (a) Contour plot of the x-ray diffuse scattering intensity distribution in the $(5.5,K,L)$ plane observed at 270 K in $TbNiC_2$. The diffuse scattering has intensity maxima at $(5.5,\eta,0)$ with $\eta \approx 0.52$ and at (5.5,0.5,0.5), which are characterized by $\boldsymbol{q}_1 = (0.5,\eta,0)$ and $\boldsymbol{q}_2 = (0.5,0.5,0.5)$, respectively. Diffuse scattering profiles measured at 255 and 270 K passing through $(5.5,\eta,0)$ are shown along the direction parallel to (b) $\boldsymbol{a}^*$, (c) $\boldsymbol{b}^*$, and (d) $\boldsymbol{c}^*$.

We found a set of satellite peaks characterized by $\boldsymbol{q}_2 = (0.5,0.5,0.5)$. A relatively intense satellite peak at (5.5,0.5,0.5) was observed along $\boldsymbol{a}^*$, $\boldsymbol{b}^*$, and $\boldsymbol{c}^*$ at several temperatures. The peak position was independent of temperature, and the value of HWHM was resolution limited below T_2. Typical profiles measured along $\boldsymbol{b}^*$ are shown in Fig. 9(c). The peak grows with decreasing temperature, but no peak is seen at 22 K (below T_N). The appearance of the $\boldsymbol{q}_2$ satellite peaks is accompanied by an increase in resistivity below T_2, and the antiferromagnetic transition involves the disappearance of the $\boldsymbol{q}_2$ satellite peaks with the sharp drop in resistivity.

Figure 10(a) shows a contour plot of the diffuse scattering intensity distribution measured at 270 K (above T_1). The intensity distribution observed in $TbNiC_2$ is similar to those observed in $GdNiC_2$ and $SmNiC_2$ [7]. The intensity distribution has maxima at (5.5,0.5,0.5) and $(5.5,\eta,0)$ with $\eta \approx 0.52$, which are given by $\boldsymbol{q}_2$ and $\boldsymbol{q}_1$, respectively. These intensity maxima indicate the presence of soft phonon modes associated with CDW instabilities. The instability with $\boldsymbol{q}_2$ develops into the long-range order in $TbNiC_2$, unlike the case in $GdNiC_2$ and $SmNiC_2$ [7]. The intensity distribution of the diffuse scattering elongates along the direction almost parallel to the c axis, passing through the $\boldsymbol{q}_2$ and $\boldsymbol{q}_1$ peaks. As shown in Figs. 10(b)–10(d), the diffuse scattering peak given

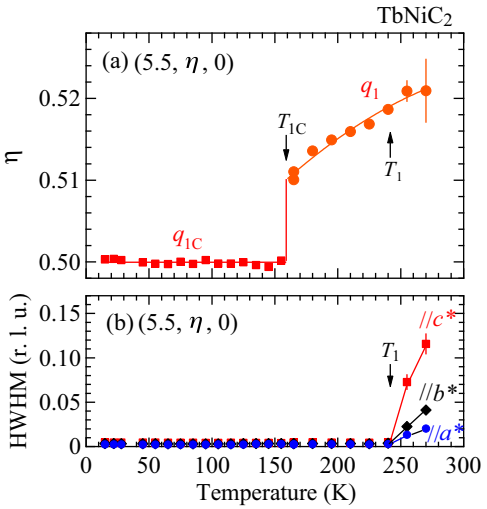

FIG. 11. Temperature dependences of (a) the η and (b) HWHM of the satellite and diffuse scattering peaks in $TbNiC_2$.

by $\boldsymbol{q}_1$, which is incommensurate only along $\boldsymbol{b}^*$, grows as the temperature decreases toward T_1.

The temperature dependence of η is shown in Fig. 11(a). The value of η decreases monotonically with decreasing temperature and then jumps to the commensurate value of 0.5 at T_{1C}. As shown in Fig. 11(b), the values of HWHM of the peak at $(5.5,\eta,0)$ measured along $\boldsymbol{a}^*$, $\boldsymbol{b}^*$, and $\boldsymbol{c}^*$ decrease with decreasing temperature and become resolution limited below T_1.

Figure 12(a) shows the temperature dependence of the integrated intensity of $(5.5,\eta,0)$ and (5.5,0.5,0), characterized

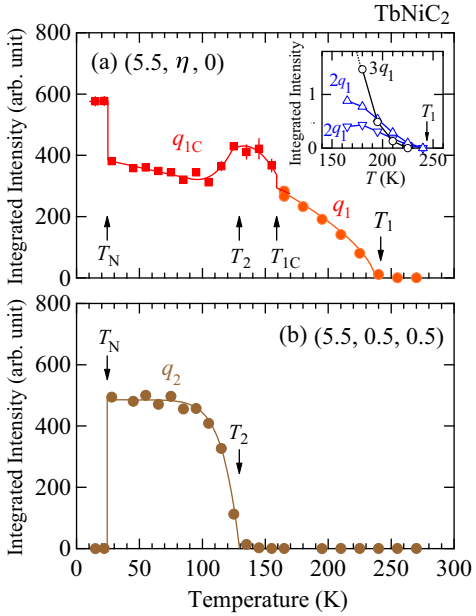

FIG. 12. (a) Temperature dependence of the integrated intensity of satellite peaks given by $\boldsymbol{q}_1$ and $\boldsymbol{q}_{1C}$ in $TbNiC_2$. The inset of (a) shows the temperature dependences of the intensities of the $2\boldsymbol{q}_1$ and $3\boldsymbol{q}_1$ satellite peaks. (b) Temperature dependence of the integrated intensity of a satellite peak given by $\boldsymbol{q}_2$.

by $\boldsymbol{q}_1$ and $\boldsymbol{q}_{1C}$, respectively. The intensity of the $\boldsymbol{q}_1$ peak increases monotonically with decreasing temperature below T_1, as expected from a conventional CDW system [1,2]. As shown in Fig. 12(b), the intensity of the $\boldsymbol{q}_2$ peak increases sharply below T_2 and discontinuously becomes zero below T_N. In contrast, the intensity of the $\boldsymbol{q}_{1C}$ satellite peak decreases below T_2, and the peak recovers its intensity and appears to be almost independent of temperature below T_N.

Magnetic peaks characterized by (0.5,0.5,0) [26,27] should appear below T_N at the same positions as the $\boldsymbol{q}_{1C}$ CDW lattice modulation peaks. However, the magnetic contribution would be negligible in this study. The satellite peak observed at (0.5,5.5,0) is relatively intense, and the ratio of its intensity to the 060 Bragg reflection intensity was approximately 10^{-2}. It is known that nonresonant x-ray magnetic scattering intensity is rarely larger than charge scattering intensity by a factor of 10^{-6} [37]. The ratio of magnetic scattering to charge scattering at (0.5,5.5,0) would be less than 10^{-4}.

The inset of Fig. 12(a) shows the intensities of the $2\boldsymbol{q}_1$ and $3\boldsymbol{q}_1$ satellite peaks. These intensities substantially increase at lower temperatures apart from T_1, indicating the squaring-up of the incommensurate lattice modulation.

IV. DISCUSSION

A. CDW transitions of RNiC$_2$

Table I shows the transition temperatures of GdNiC$_2$, TbNiC$_2$, and SmNiC$_2$ [7] determined from the temperature dependence of the electrical resistivity, and the wave vector characterizing the CDW phase below each transition temperature. The values of T_C and T_N are in good agreement with those determined by magnetic measurements [15,24,25]. No apparent anomalies in the magnetic susceptibility were observed at T_1 or T_{1C} [15,24,25]. These results indicate that the changes in the Pauli paramagnetism are too small to be detected in comparison with the large moment contributions of Gd, Tb, and Sm ions.

TABLE I. Transition temperatures of RNiC$_2$ (R = Sm [7], Gd, and Tb) determined from the observed temperature dependence of the electrical resistivity. The wave vector characterizing the CDW phase is shown below each transition temperature: $\boldsymbol{q}_1 = (0.5,\eta,0)$, $\boldsymbol{q}_{1C} = (0.5,0.5,0)$, and $\boldsymbol{q}_2 = (0.5,0.5,0.5)$.

	SmNiC$_2$	GdNiC$_2$	TbNiC$_2$
T_1 (K)	148	205	243
Wave vector	$\boldsymbol{q}_1$	$\boldsymbol{q}_1$	$\boldsymbol{q}_1$
T_{1C} (K)	–	90 (heating)	160 (heating)
	–	76 (cooling)	157 (cooling)
Wave vector		$\boldsymbol{q}_{1C}$	$\boldsymbol{q}_{1C}$
T_2 (K)	–	–	128
Wave vector			$\boldsymbol{q}_{1C}$ and $\boldsymbol{q}_2$
T_N (K)	–	22.3 (heating)	25.2 (heating)
	–	21.5 (cooling)	24.7 (cooling)
Wave vector		$\boldsymbol{q}_{1C}$	$\boldsymbol{q}_{1C}$
T_C (K)	17.7	–	–
Wave vector	–		

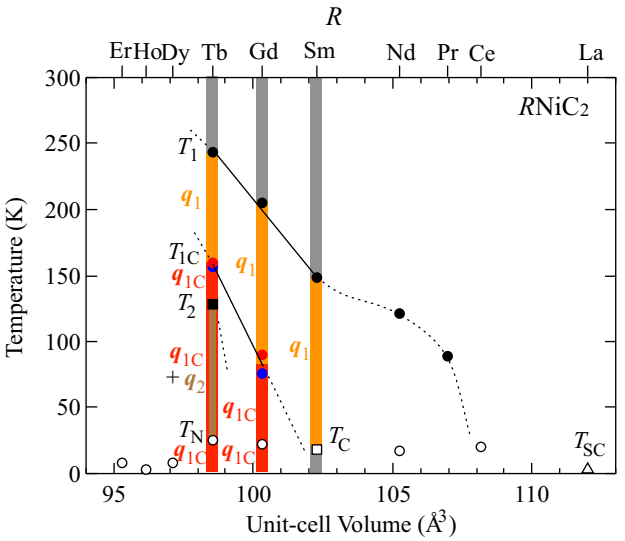

FIG. 13. CDW transition temperatures T_1, T_{1C}, and T_2 are plotted against the room temperature unit-cell volume in RNiC$_2$. The gray, orange, and red lines represent the prototypical phase, the CDW phase with $\boldsymbol{q}_1 = (0.5,\eta,0)$, and the CDW phase with $\boldsymbol{q}_{1C} = (0.5,0.5,0)$, respectively. The phase modulated with $\boldsymbol{q}_{1C}$ and $\boldsymbol{q}_2 = (0.5,0.5,0.5)$, stabilized in TbNiC$_2$, is denoted by the red and brown line. Values of T_1 reported for NdNiC$_2$ and PrNiC$_2$ are also plotted [35,38]. Ferromagnetic (T_C), antiferromagnetic (T_N), and superconducting (T_{SC}) transition temperatures [15,19–30] are denoted by the open square, open circles, and open triangle, respectively.

In Fig. 13 we plot the transition temperatures against the room temperature unit-cell volume [15,22–26]. A similar phase diagram can be drawn as a function of the ionic radius of R^{3+} or the atomic number of R instead of the unit-cell volume, because the RNiC$_2$ compounds follow a normal lanthanide contraction [15]. Magnetic [15,19–28], CDW [35,38], and superconducting [29,30] transition temperatures reported in other RNiC$_2$ compounds are also plotted in Fig. 13.

The values of T_1 obtained for TbNiC$_2$, GdNiC$_2$, and SmNiC$_2$ appear to decrease linearly with increasing unit-cell volume. This dependence would appear to contradict the idea that the band broadening due to the contraction of volume results in the suppression of CDW. The values of T_1 decrease with higher unit-cell volumes as shown by the dashed curve, in accordance with the previously reported results for the T_1 of NdNiC$_2$ and PrNiC$_2$, and in agreement with the absence of experimental evidence of the CDW formation in CeNiC$_2$ and LaNiC$_2$ [15,29,30,34,35,38]. The values of T_{1C} seem to decrease with the unit-cell volume. It can be extrapolated on the basis of the plots of T_1 and T_{1C} that DyNiC$_2$, HoNiC$_2$, and ErNiC$_2$ also exhibit similar transitions. The electrical resistivity and x-ray measurements of these compounds are necessary to determine whether or not T_1, T_{1C}, and T_2 are present.

The CDW state below T_C or T_N appears not to follow the simple unit-cell volume dependence. The prototypical phase, denoted by the gray lines, is stabilized again below T_C in SmNiC$_2$. The phase with $\boldsymbol{q}_{1C}$, represented by the red line, is stable below T_N in GdNiC$_2$ and TbNiC$_2$. In GdNiC$_2$, the CDW lattice modulation with $\boldsymbol{q}_{1C}$ is reduced below T_N. Similar

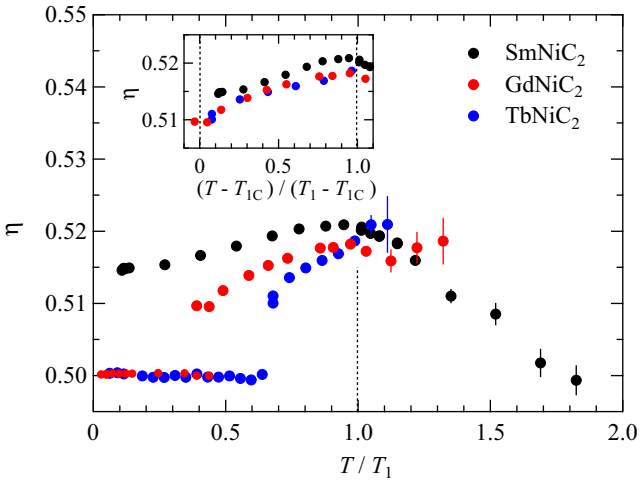

FIG. 14. Values of η obtained for $GdNiC_2$, $TbNiC_2$, and $SmNiC_2$ [7] are plotted as a function of the reduced temperature T/T_1. The inset shows a similar plot against another reduced temperature $(T - T_{1C})/(T_1 - T_{1C})$. In $SmNiC_2$, T_{1C} is assumed to be -1.4 K.

suppression below T_N was reported in $NdNiC_2$ [38]. The effects of the magnetic transitions on the CDWs are discussed in Sec. IV C.

The observed values of the electrical resistivity below T_C or T_N are qualitatively consistent with the remaining CDW orders. The values of the electrical resistivity below T_N in $GdNiC_2$ (Fig. 3) and $TbNiC_2$ (Fig. 8) are higher than that below T_C in $SmNiC_2$ (Fig. 1), while the three compounds have similar values above T_1. For instance, the values of ρ_c at about 3 K in $GdNiC_2$ and $TbNiC_2$ are about 5 and 11 times higher than that in $SmNiC_2$, respectively. The antiferromagnetic phase of $TbNiC_2$ has the highest resistivity in accordance with the existence of the $\boldsymbol{q}_{1C}$ CDW order. The weakened $\boldsymbol{q}_{1C}$ CDW below T_N in $GdNiC_2$ would result in a lower resistivity than that in $TbNiC_2$. The absence of the long-range and short-range lattice modulations in the ferromagnetic state of $SmNiC_2$ indicates that the Fermi surface is entirely restored, resulting in the lowest resistivity. First-principles calculations [8,39] also indicated the destruction of the CDW below T_C. In the photoemission spectroscopy [9] of $SmNiC_2$, however, the gap opening due to the CDW formation below T_1 was reported to remain even below T_C. This contradiction remains to be understood.

The values of η observed in $GdNiC_2$, $TbNiC_2$, and $SmNiC_2$ [7] show a similar temperature dependence. The values of η are plotted as a function of the reduced temperature T/T_1 in Fig. 14. They vary from about 0.52 to 0.50 below $T/T_1 = 1$. A similar plot is shown in the inset of Fig. 14 as a function of another reduced temperature $(T - T_{1C})/(T_1 - T_{1C})$. The hypothetical value of T_{1C} for $SmNiC_2$ is estimated to be -1.4 K on the assumption that T_{1C} decreases linearly with the unit-cell volume. The values of η appear to follow the same curve in the reduced-temperature range between 0 (T_{1C}) and 1 (T_1).

B. CDW instability

As described in Sec. III and Ref. [7], the diffuse scatterings observed above T_1 in $GdNiC_2$, $TbNiC_2$, and $SmNiC_2$ are analogous in terms of their intensity distributions. This suggests that these compounds have similar Fermi surfaces, because the thermal diffuse scattering reflects the phonon dispersion relation associated with the electronic structures. Figure 15(a) schematically illustrates the observed intensity distribution on a reciprocal lattice plane (H,K,L) with a half-integer H value. The Brillouin zone of the prototypical A-centered orthorhombic lattice, which is also shown in the inset, is drawn

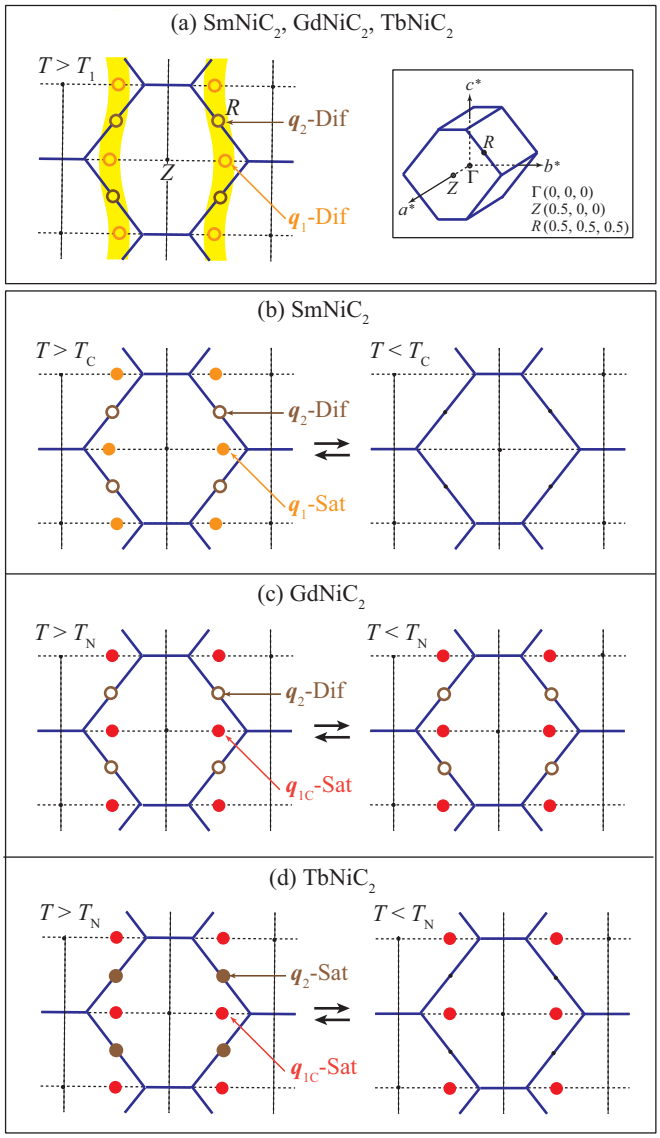

FIG. 15. (a) Schematic illustration of the diffuse scattering observed above T_1 in $SmNiC_2$, $GdNiC_2$, and $TbNiC_2$ on a reciprocal plane (H,K,L) with a half-integer H value. Blue lines represent the first Brillouin zone, which is also shown in the inset. Wavy yellow lines indicate the intensity distribution of the diffuse scattering. Orange and brown open circles represent the diffuse scattering peaks centered at positions given by $\boldsymbol{q}_1$ ($\boldsymbol{q}_1$-Dif) and $\boldsymbol{q}_2$ ($\boldsymbol{q}_2$-Dif), respectively. (b) Schematic illustrations of positions of satellite peaks given by $\boldsymbol{q}_1$ ($\boldsymbol{q}_1$-Sat) and diffuse scattering peaks given by $\boldsymbol{q}_2$ observed above and below T_C in $SmNiC_2$. (c) Similar schematic illustrations above and below T_N in $GdNiC_2$, and (d) above and below T_N in $TbNiC_2$. Red and brown filled circles denote the satellite peaks given by $\boldsymbol{q}_{1C}$ ($\boldsymbol{q}_{1C}$-Sat) and $\boldsymbol{q}_2$ ($\boldsymbol{q}_2$-Sat), respectively.

by the blue lines. The diffuse scattering has intensity maxima at the positions given by $\boldsymbol{q}_1$ and $\boldsymbol{q}_2$, which are denoted by orange and brown open circles, respectively. The intensity maxima probably arise from the phonon softening due to the CDW instabilities, which are supported by the calculated electronic band structure [8] that shows the Fermi surface nesting and the divergence of the electronic susceptibility for both $\boldsymbol{q}_1$ and $\boldsymbol{q}_2$. The broad diffuse scattering, denoted by the yellow curves in Fig. 15(a), was observed well above T_1, indicating a pronounced softening of the phonon branch or a weak correlation along $\boldsymbol{c}$.

C. Effects of magnetic transitions on CDWs

First, we summarize our experimental results relevant to the effects of the magnetic transitions on CDWs. Figures 15(b)–15(d) illustrate the presence of the satellite and diffuse scattering peaks above and below the magnetic transition temperatures in $SmNiC_2$ [7], $GdNiC_2$, and $TbNiC_2$, respectively. In $SmNiC_2$, the $\boldsymbol{q}_1$ satellite peaks (denoted by the orange filled circles) and the $\boldsymbol{q}_2$ diffuse scattering peaks (brown open circles) disappear below T_C. In $GdNiC_2$, the $\boldsymbol{q}_{1C}$ satellite peaks (red filled circles) and the $\boldsymbol{q}_2$ diffuse scattering peaks remain even below T_N. The $\boldsymbol{q}_{1C}$ peaks, however, become less intense below T_N, while the $\boldsymbol{q}_2$ diffuse scattering peaks show no anomalous changes. In $TbNiC_2$, the $\boldsymbol{q}_2$ satellite peaks (brown filled circles) disappear below T_N, while the $\boldsymbol{q}_{1C}$ satellite peaks persist. A feature common to the three compounds is that the magnetic transitions have unfavorable effects on CDWs: the long-range CDW orders and/or short-range correlation are suppressed or vanish.

At present, we can offer no definitive interpretation of the microscopic mechanism of the interplay between the CDW and magnetic orders in $RNiC_2$. However, this interplay would result from interactions among the crystal lattice, conduction electrons, and $4f$ magnetic moments, such as the electron-lattice, RKKY, and magnetoelastic interactions. The interrelations between the magnetic structures and the nesting properties and the role of the magnetoelastic interaction are discussed below.

The detailed effects of the magnetic transitions on CDWs depend on the compounds or types of magnetic order. The first-principles calculations demonstrated the suppression of the nesting properties of the Fermi surface with the splitting of conduction bands in the ferromagnetic state of $SmNiC_2$ [8,39]. The antiferromagnetic order should also modify the electronic structures and change the nesting properties of the Fermi surface. Note that, in $TbNiC_2$, the antiferromagnetic order coexists with the CDW order given by $\boldsymbol{q}_{1C}$, which is the same as the magnetic wave vector (0.5,0.5,0) [26,27]. This indicates that the nesting condition associated with $\boldsymbol{q}_{1C}$ remains unchanged through the antiferromagnetic transition. In contrast, the CDW order given by $\boldsymbol{q}_2$ disappears below T_N. In $SmNiC_2$, the CDW order given by $\boldsymbol{q}_1$ is destroyed by the ferromagnetic order, which is characterized by the magnetic wave vector (0,0,0). In $TbNiC_2$ and $SmNiC_2$, the magnetic transition has an unfavorable effect on the CDW order associated with the nesting wave vector that is distinct from the magnetic wave vector. Determinations of the magnetic structure of $GdNiC_2$ and the electronic structures in the antiferromagnetic state of $GdNiC_2$ and that of $TbNiC_2$ are needed to clarify the interrelations between the magnetic structures and the nesting properties of the Fermi surface.

According to the neutron diffraction experiments on $TbNiC_2$, the magnetic satellite peak given by (0.5,0.5,0) increases its intensity gradually with decreasing temperature below T_N [26,27]. In contrast, as shown in Figs. 12(a) and 12(b), the $\boldsymbol{q}_2$ CDW satellite peak abruptly disappears at T_N, and the $\boldsymbol{q}_{1C}$ CDW satellite intensity is almost independent of temperature below T_N. The difference between the temperature dependence of the magnetic peak and those of the CDW peaks suggests the indirect coupling between the order parameters of antiferromagnetism and CDWs.

The first-principles calculations for $LaNiC_2$ indicate the poor nesting of the Fermi surface, which is attributable to the lattice constants rather than the rare-earth substitution [8]. Anisotropic changes in the lattice constants at a magnetic transition temperature through the magnetoelastic interaction might be one of the reasons for the unfavorable effects on the nesting conditions. In fact, the discontinuous changes in the lattice constants at T_C in $SmNiC_2$ and those at T_N in $TbNiC_2$ have been reported [35]. In contrast, the lattice constants of $GdNiC_2$ showed small and continuous changes around T_N [35], which would be one of the reasons why the CDW order does not disappear below T_N. In Gd^{3+}, the orbital angular momentum vanishes ($L = 0$), and the magnetic properties are expected to be isotropic. The magnetoelastic interaction due to the change in the crystal field caused by the changes in the lattice constants is negligible [35]. The evolution of the magnetic order would produce a small lattice deformation originating from the exchange interaction depending on the distance between the magnetic ions. This deformation might result in the suppression of the $\boldsymbol{q}_{1C}$ CDW accompanied by the rapid decrease in the resistivity below T_N in $GdNiC_2$.

The application of external magnetic fields probably induces exotic phenomena related to CDW transitions via magnetic transitions. The $\boldsymbol{q}_1$ CDW order of $SmNiC_2$ is destroyed by an external magnetic field, accompanied by large negative magnetoresistance [40]. A previously reported field-temperature phase diagram of $GdNiC_2$ is composed of many phases [41], suggesting a degenerate manifold of ground states due to frustration. Investigations of the structural and magnetic properties of $RNiC_2$ in magnetic fields would provide valuable information about the interplay between CDW and magnetism.

D. Modulation with $\boldsymbol{q}_{1C}$ and $\boldsymbol{q}_2$

We propose a possible displacement pattern of the modulated structure with $\boldsymbol{q}_{1C}$ and $\boldsymbol{q}_2$ observed in the temperature range between T_N and T_2 in $TbNiC_2$. According to the structure analysis for the incommensurate $\boldsymbol{q}_1$ modulated phase of $SmNiC_2$ [14], Ni atoms, which are displaced parallel to $\boldsymbol{a}$, exhibit the largest modulation amplitude, suggesting that they carry the CDW. For the $\boldsymbol{q}_{1C}$ and $\boldsymbol{q}_2$ modulations, we consider only the displacement of Ni atoms, and assume that the amplitudes of the $\boldsymbol{q}_{1C}$ and $\boldsymbol{q}_2$ modulations are parallel to $\boldsymbol{a}$. When the modulations are sinusoidal plane waves, the

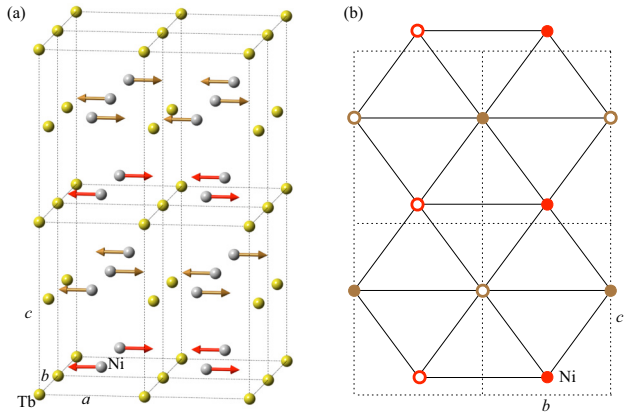

FIG. 16. (a) A possible pattern of the atomic displacements of Ni atoms due to the modulations with $\boldsymbol{q}_{1C} = (0.5,0.5,0)$, $\boldsymbol{q}_{2^+} = (0.5,0.5,0.5)$, and $\boldsymbol{q}_{2^-} = (0.5,-0.5,0.5)$ in a $2a \times 2b \times 2c$ cell. Carbon atoms are not shown for clarity. (b) The displacements of Ni atoms on the plane with $x = 0.5$ perpendicular to $\boldsymbol{a}$ are represented by the open and filled circles.

displacement of the jth atom is given by

$$u^x(\boldsymbol{r}_j) = \sum_\alpha A^x_\alpha \sin(\boldsymbol{q}_\alpha \cdot \boldsymbol{r}_j + \phi_\alpha),$$

where $\boldsymbol{q}_\alpha$, A^x_α, and ϕ_α are the wave vector, modulation amplitude, and phase, respectively. It should be noted that the wave vectors $\boldsymbol{q}_{2^+} = (0.5,0.5,0.5)$ and $\boldsymbol{q}_{2^-} = (0.5,-0.5,0.5)$ are required for an indexing of the observed reflections that have been represented by $\boldsymbol{q}_2$, based on the A-centered orthorhombic lattice, in which fundamental Bragg reflections (h,k,l) with $k + l =$ odd are extinct. The possibility that reflections given by $\boldsymbol{q}_{2^-}$ come from twin variants with $\boldsymbol{q}_{2^+}$ is not taken into consideration. The superposition of the modulations involves the components of $\boldsymbol{q}_{2^+}$, $\boldsymbol{q}_{2^-}$, and $\boldsymbol{q}_{1C}$.

Figure 16(a) shows a possible pattern of the displacement directions of Ni atoms, which are represented by the arrows, in a $2a \times 2b \times 2c$ cell. This pattern is based on the assumptions that the $\boldsymbol{q}_{2^+}$ and $\boldsymbol{q}_{2^-}$ modulations have the same modulation amplitude, and that ϕ_{1C} is chosen to be $\pi/2$. The red arrows in the layer containing Ni atoms at $(0.5,0.5,z)$ with $z \approx 0.11$ indicate displacements only of the $\boldsymbol{q}_{1C}$ modulation, because the contributions from the $\boldsymbol{q}_{2^+}$ and $\boldsymbol{q}_{2^-}$ modulations cancel out. In contrast, the contribution from the $\boldsymbol{q}_{1C}$ modulation becomes zero in the neighboring layer, and the displacements denoted by the brown arrows originate from the $\boldsymbol{q}_{2^+}$ and $\boldsymbol{q}_{2^-}$ modulations. Figure 16(b) shows the displacement directions of Ni atoms on the plane with $x = 0.5$ perpendicular to $\boldsymbol{a}$. The open and filled circles represent the displacement directions toward $\boldsymbol{a}$ and $-\boldsymbol{a}$, respectively. The prototypic structure with the A-centered orthorhombic lattice can be described as a distorted hexagonal lattice, and Ni atoms are situated on a distorted triangular lattice. Each triangle is composed of two filled (open) circles and one open (filled) circle.

Some of the assumptions we made in order to demonstrate the displacement pattern are conjectural. Nevertheless, the pattern provides a possible interpretation of the CDWs of RNiC$_2$ in terms of frustration. According to Wölfel *et al.* [14], the symmetry of the A center appears to provide frustration between the $\boldsymbol{q}_{1C}$ modulations on Ni chains along $\boldsymbol{a}$ in neighboring layers. In the pattern shown in Fig. 16, the amplitude given by $\boldsymbol{q}_{1C}$ becomes zero on every second layer. In these layers, Ni atoms are displaced with the modulations with $\boldsymbol{q}_{2^+}$ and $\boldsymbol{q}_{2^-}$.

A more realistic structure model will be needed. The displacements of Sm and C$_2$ atoms should also be taken into account. Structure determinations of not only the $\boldsymbol{q}_{1C}$ and $\boldsymbol{q}_2$ phase but also the $\boldsymbol{q}_{1C}$ phase are needed to clarify the mechanism of the CDW transitions.

In GdNiC$_2$ and SmNiC$_2$ [7], the $\boldsymbol{q}_2$ short-range correlation does not develop into the long-range order. The diffuse scattering observed above T_1, as shown in Fig. 15(a), elongates almost along $\boldsymbol{c}^*$ and not along the axes corresponding to the distorted hexagonal (triangular) lattice. The suppression of the $\boldsymbol{q}_2$ long-range order and weaker correlation between layers perpendicular to $\boldsymbol{c}$ would be ascribed to the frustration described above.

V. CONCLUSIONS

Electrical resistivity, x-ray diffraction, and x-ray diffuse scattering measurements have been performed on GdNiC$_2$ and TbNiC$_2$. An incommensurate CDW characterized by $\boldsymbol{q}_1 = (0.5,\eta,0)$ is formed below T_1, where the electrical resistivity shows a sharp inflection. The value of η is locked into the commensurate value of 0.5 at T_{1C}. In TbNiC$_2$, the long-range order with $\boldsymbol{q}_2 = (0.5,0.5,0.5)$ additionally evolves below T_2. The diffuse scattering observed above T_1 shows a characteristic intensity distribution. The intensity maxima of the diffuse scattering indicate the phonon softening leading to the CDW transitions characterized by $\boldsymbol{q}_1$ and $\boldsymbol{q}_2$. The CDW transition sequences are similar in RNiC$_2$ compounds (R = rare earth). The magnetic transitions have unfavorable effects on CDWs. In GdNiC$_2$, the intensity of the satellite peak given by $\boldsymbol{q}_{1C} = (0.5,0.5,0)$ decreases below T_N, accompanied by a sharp decrease in electrical resistivity. In TbNiC$_2$, the electrical resistivity discontinuously changes at T_N, below which the satellite peaks given by $\boldsymbol{q}_2$ suddenly disappear, while those by $\boldsymbol{q}_{1C}$ remain. We propose a possible displacement pattern of the modulated structure characterized by $\boldsymbol{q}_{1C}$ and $\boldsymbol{q}_2$ in terms of frustration. The RNiC$_2$ could be described as a novel CDW system characterized by the charge frustration and the interplay between CDW and magnetism.

ACKNOWLEDGMENTS

We are grateful to N. Wakabayashi and M. Kosaka for their helpful advice and to Y. Yamasaki, K. Yokota, and Y. Nogami for their help in x-ray diffraction experiments. The synchrotron radiation experiments were performed at SPring-8 with the approval of the Japan Synchrotron Radiation Research Institute (JASRI) (Proposals 2005B0300 and 2006A1255) and at the Photon Factory with the approval of the Photon Factory Program Advisory Committee (Proposals 2009G025, 2011G101, and 2013G106). This work was supported by JSPS KAKENHI Grant No. 22540373.

[1] G. Grüner, *Density Waves in Solids* (Addison-Wesley, Reading, MA, 1994).

[2] G. Grüner, Rev. Mod. Phys. **60**, 1129 (1988).

[3] F. Galli, S. Ramakrishnan, T. Taniguchi, G. J. Nieuwenhuys, J. A. Mydosh, S. Geupel, J. Lüdecke, and S. van Smaalen, Phys. Rev. Lett. **85**, 158 (2000).

[4] F. Galli, R. Feyerherm, R. W. A. Hendrikx, S. Ramakrishnan, G. J. Nieuwenhuys, and J. A. Mydosh, Phys. Rev. B **62**, 13840 (2000).

[5] F. Galli, R. Feyerherm, R. W. A. Hendrikx, E. Dudzik, G. J. Nieuwenhuys, S. Ramakrishnan, S. D. Brown, S. van Smaalen, and J. A. Mydosh, J. Phys.: Condens. Matter **14**, 5067 (2002).

[6] S. van Smaalen, M. Shaz, L. Palatinus, P. Daniels, F. Galli, G. J. Nieuwenhuys, and J. A. Mydosh, Phys. Rev. B **69**, 014103 (2004).

[7] S. Shimomura, C. Hayashi, G. Asaka, N. Wakabayashi, M. Mizumaki, and H. Onodera, Phys. Rev. Lett. **102**, 076404 (2009).

[8] J. Laverock, T. D. Haynes, C. Utfeld, and S. B. Dugdale, Phys. Rev. B **80**, 125111 (2009).

[9] T. Sato, S. Souma, K. Nakayama, T. Takahashi, S. Shimomura, and H. Onodera, J. Phys. Soc. Jpn. **79**, 044707 (2010).

[10] D. Ahmad, B. H. Min, G. I. Min, S.-I. Kimura, J. Seo, and Y. S. Kwon, Phys. Status Solidi B **252**, 2662 (2015).

[11] O. I. Bodak and E. P. Marussin, Dokl. Akad. Nauk Ukr. SSR, Ser. A **12**, 1048 (1979).

[12] K. N. Semenenko, A. A. Putyatin, I. V. Nikol'skaya, and V. V. Burnasheva, Russ. J. Inorg. Chem. **28**, 943 (1983).

[13] W. Jeitschko and M. Gerss, J. Less-Common Met. **116**, 147 (1986).

[14] A. Wölfel, L. Li, S. Shimomura, H. Onodera, and S. van Smaalen, Phys. Rev. B **82**, 054120 (2010).

[15] H. Onodera, Y. Koshikawa, M. Kosaka, M. Ohashi, H. Yamauchi, and Y. Yamaguchi, J. Magn. Magn. Mater. **182**, 161 (1998).

[16] M. Mizumaki, N. Kawamura, and H. Onodera, Phys. Status Solidi C **3**, 2767 (2006).

[17] J. H. Kim, J.-S. Rhyee, and Y. S. Kwon, Phys. Rev. B **86**, 235101 (2012).

[18] B. Woo, S. Seo, E. Park, J. H. Kim, D. Jang, T. Park, H. Lee, F. Ronning, J. D. Thompson, V. A. Sidorov, and Y. S. Kwon, Phys. Rev. B **87**, 125121 (2013).

[19] J. Yakinthos, P. Kotsanidis, W. Schäfer, and G. Will, J. Magn. Magn. Mater. **89**, 299 (1990).

[20] J. Yakinthos, P. Kotsanidis, W. Schäfer, and G. Will, J. Magn. Magn. Mater. **102**, 71 (1991).

[21] J. Yakinthos, P. Kotsanidis, W. Schäfer, W. Kockelmann, G. Will, and W. Reimers, J. Magn. Magn. Mater. **136**, 327 (1994).

[22] H. Onodera, M. Ohashi, H. Amanai, S. Matsuo, H. Yamauchi, Y. Yamaguchi, S. Funahashi, and Y. Morii, J. Magn. Magn. Mater. **149**, 287 (1995).

[23] Y. Koshikawa, H. Onodera, M. Kosaka, H. Yamauchi, M. Ohashi, and Y. Yamaguchi, J. Magn. Magn. Mater. **173**, 72 (1997).

[24] S. Matsuo, H. Onodera, M. Kosaka, H. Kobayashi, M. Ohashi, H. Yamauchi, and Y. Yamaguchi, J. Magn. Magn. Mater. **161**, 255 (1996).

[25] H. Onodera, N. Uchida, M. Ohashi, H. Yamauchi, Y. Yamaguchi, and N. Sato, J. Magn. Magn. Mater. **137**, 35 (1994).

[26] N. Uchida, H. Onodera, M. Ohashi, Y. Yamaguchi, N. Sato, and S. Funahashi, J. Magn. Magn. Mater. **145**, L16 (1995).

[27] J. Yakinthos, P. Kotsanidis, W. Schäfer, and G. Will, J. Magn. Magn. Mater. **81**, 163 (1989).

[28] W. Schäfer, G. Will, J. Yakinthos, and P. Kotsanidis, J. Alloys Compd. **180**, 251 (1992).

[29] W. Lee, H. Zeng, Y. Yao, and Y. Chen, Physica C **266**, 138 (1996).

[30] V. K. Pecharsky, L. L. Miller, and K. A. Gschneidner, Phys. Rev. B **58**, 497 (1998).

[31] A. D. Hillier, J. Quintanilla, and R. Cywinski, Phys. Rev. Lett. **102**, 117007 (2009).

[32] A. Subedi and D. J. Singh, Phys. Rev. B **80**, 092506 (2009).

[33] I. Hase and T. Yanagisawa, J. Phys. Soc. Jpn. **78**, 084724 (2009).

[34] Y. Hirose, T. Kishino, J. Sakaguchi, Y. Miura, F. Honda, T. Takeuchi, E. Yamamoto, Y. Haga, H. Harima, R. Settai, and Y. Ōnuki, J. Phys. Soc. Jpn. **81**, 113703 (2012).

[35] M. Murase, A. Tobo, H. Onodera, Y. Hirano, T. Hosaka, S. Shimomura, and N. Wakabayashi, J. Phys. Soc. Jpn. **73**, 2790 (2004).

[36] P. Brüesch, *Phonons: Theory and Experiments II* (Springer, Berlin, 1986).

[37] D. Gibbs, J. P. Hill, and C. Vettier, *Third-Generation Hard X-ray Synchrotron Radiation Sources*, edited by D. M. Mills (Wiley-Interscience, New York, 2002), Chap. 8, p. 267.

[38] N. Yamamoto, R. Kondo, H. Maeda, and Y. Nogami, J. Phys. Soc. Jpn. **82**, 123701 (2013).

[39] J. N. Kim, C. Lee, and J.-H. Shim, New J. Phys. **15**, 123018 (2013).

[40] N. Hanasaki, Y. Nogami, M. Kakinuma, S. Shimomura, M. Kosaka, and H. Onodera, Phys. Rev. B **85**, 092402 (2012).

[41] N. Hanasaki, K. Mikami, S. Torigoe, Y. Nogami, S. Shimomura, M. Kosaka, and H. Onodera, J. Phys.: Conf. Ser. **320**, 012072 (2011).